



Quinacridone based 2D covalent organic frameworks as efficient photocatalysts for aerobic oxidative Povarov reaction

Ziling Liu^a, Xiao Yang^a, Zongfan Yang^a, Xi Su^a, Zhen Xie^{a,b}, Weihua Chen^c, Wenqin Zhang^{a,*}, Long Chen^{a,d,**}

^a Department of Chemistry, Tianjin Key Laboratory of Molecular Optoelectronic Science, Tianjin University, Tianjin 300072, China

^b Province Key Laboratory of Natural Medicine and Immuno-Engineering, Henan University, Kaifeng 475004, Henan, China

^c College of Chemistry and Green Catalysis Center, Zhengzhou University, 450001 Henan, China

^d State Key Laboratory of Supramolecular Structure and Materials, College of Chemistry, Jilin University, Changchun 130012, China

ARTICLE INFO

Keywords:

Quinacridone
Covalent organic frameworks
Large pore size (> 4.7 nm)
Photocatalytic activity
Povarov reaction

ABSTRACT

Quinacridone (QA) derivatives, one of cost-effective dyes with intriguing optical activity, have been extensively investigated in many fields such as organic light-emitting diodes, organic solar cells, and photocatalysis. Herein, a new QA-monomer (QA-PCHO) with a zigzag configuration was synthesized via *N*-arylation of benzene halide and quinacridone. The new monomer could enrich eventual structural diversity of the corresponding covalent organic frameworks (COFs). And based on the precursor, we developed two new QA-based 2D imine COFs with large pore size (> 4.7 nm) which exhibited superior photocatalytic activity toward Povarov reaction with broad substrate scopes and excellent functional group compatibility.

1. Introduction

Covalent organic frameworks (COFs) feature long range ordering, regular open porous nanochannels, high stability and abundant accessible active sites [1], which can be served as a promising platform for heterogeneous catalysts [2–7]. Rational combination of compatible knots and linkers not only realizes the successful construction of multitudinous COF skeletons with periodic networks [8–10], but also regulates the electronic structures and photophysical properties of the corresponding frameworks [11–14]. To date, COFs have shown excellent activity in organic transformations [15], asymmetric catalysis [16, 17], photocatalytic hydrogen production, photocatalytic reduction [18] and water splitting [19–22]. In order to optimize the catalytic performance, various microporous COFs have been widely designed and synthesized [23,24], while the reports on COFs with large pore size (> 4.7 nm) is relatively rare. COFs with large-pore structure are more conducive to the adsorption [25], the diffusion of substrates and mass transport in heterogeneous catalysis, which is beneficial for the catalytic reaction [26].

Quinacridone (QA) was originally used as pigment for plastics and rubber industry taking advantage of their vivid color, exceptional

weather fastness, excellent environmental stability, low toxicity, and ability to be mass-produced. In addition, due to their derivatives exhibit promising photophysical properties [27], quinacridone chromophore not only has attracted significant research attention in organic light-emitting diodes (OLEDs) [28], but also has been widely employed on photocatalytic hydrogen production [29], photocatalytic reduction of CO₂ [30], ion detection [31] and solar cells [32,33]. Alkylation and arylation at the amide nitrogens are the simplest methods for the functionalization of commercially available quinacridone [34], which could greatly improve its processibility, molecular stacking and photophysical properties [35].

2. Experimental

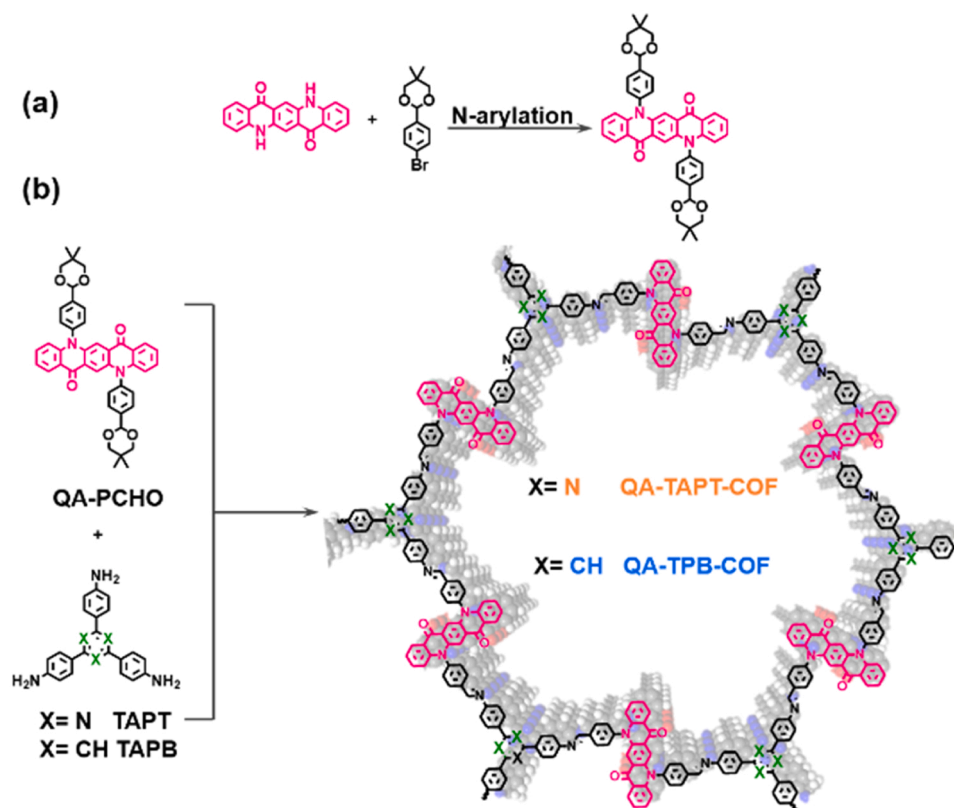
2.1. Synthesis of QA-COFs

Synthesis of QA-TAPT-COF: To a 10 mL Schlenk tube, 5,12-bis(4-(5,5-dimethyl-1,3-dioxan-2-yl)phenyl)-5,12-dihydroquinolino[2,3-*b*]acridine-7,14-dione (QA-PCHO) (50.0 mg, 0.072 mmol), 1,3,5-tris(4-aminophenyl)triazine (TAPT) (17.0 mg, 0.048 mmol), 1,2-dichlorobenzene/*n*-butanol (*o*-DCB/*n*-BuOH = 0.4 mL/ 0.6 mL) were added. The

* Corresponding author.

** Corresponding author at: Department of Chemistry, Tianjin Key Laboratory of Molecular Optoelectronic Science, Tianjin University, Tianjin 300072, China.

E-mail addresses: zhangwenqin@tju.edu.cn (W. Zhang), long.chen@tju.edu.cn (L. Chen).



Scheme 1. (a) The synthetic route of QA-PCHO. (b) The solvothermal synthesis of QA-TAPT-COF and QA-TPB-COF.

mixture was sonicated for 2 min, 6 M AcOH (0.20 mL) was added and sonicated for another 2 min. The mixture was degassed by three freeze-pump-thaw cycles. After warming to room temperature, the tube was sealed under reduced pressure and heated to 150 °C for 5 days. After cooling down to temperature, the precipitate was collected, washed with *N,N*-dimethylformamide (DMF), tetrahydrofuran (THF) and ethyl alcohol (EtOH), and dried in a vacuum chamber at 120 °C overnight to obtain QA-TAPT-COF (42.4 mg) as a red solid in 82% yield.

Synthesis of QA-TPB-COF: To a 10 mL Schlenk tube, QA-PCHO (20.8 mg, 0.03 mmol), 1,3,5-tris(4-aminophenyl)benzene (TAPB) (7.1 mg, 0.02 mmol) and *o*-DCB/*n*-BuOH (0.3 mL/ 0.7 mL) were added. The mixture was sonicated for 2 min, 6 M AcOH (0.15 mL) was added and sonicated for another 2 min. The mixture was degassed by three freeze-pump-thaw cycles. After warming to room temperature, the tube was sealed under reduced pressure and heated to 150 °C for 3 days. After cooling down to room temperature, the precipitate was collected, washed with DMF, THF and EtOH, and dried in a vacuum chamber at 120 °C overnight to afford QA-TPB-COF (20.1 mg) as a red solid in 93% yield.

2.2. Characterization

^1H and ^{13}C nuclear magnetic resonance (NMR) spectra of QA-PCHO were carried out on a Bruker AVANCE III-400 MHz NMR spectrometer. High-resolution mass spectra (HR-MS) of QA-PCHO was performed on Thermo Fisher Q Exactive Mass Spectrometer. Fourier Transform Infrared (FT-IR) spectra were recorded in reflection mode on a Bruker Alpha spectrometer with a scan range of 400–4000 cm^{-1} . The solid-state ^{13}C Cross-Polarization with total suppression of spinning sidebands (CP-TOSS) spectra were recorded on JEOL JNM ECZ600R (600 MHz) solid state NMR spectrometer with a 3.2 mm double resonance MAS probe and at a MAS rate of 10.0 kHz with a contact time of 3 ms (ramp 100) and a pulse delay of 5 s. UV–vis spectra were measured on PerkinElmer Lambda 750 spectrometer, the sweep range was set from 270 to 800 nm.

The thermal stabilities were evaluated by thermogravimetric analysis (TGA) with a differential thermal analysis instrument (TA Instruments TGA Q50–1918 analyzer) over the temperature range from 30° to 800°C. The analysis was carried out under N_2 atmosphere with a heating rate of 10 °C min^{-1} using an empty Al_2O_3 crucible as the reference. Powder X-ray diffraction (PXRD) measurements were carried out on X-ray diffractometer model RIGAKU SMARTLAB9KW diffractometer (Japan) at 45 kV, 200 mA with a Cu-target tube and a graphite monochromator. Field emission scanning electron microscopy (FE-SEM) measurements were performed on a Hitachi Limited Model SU8010 microscope operating at an accelerating voltage of 5.0 kV. The porosities were evaluated by nitrogen sorption isotherms at 77 K using a Bel Japan Inc. model BELSOPR-max analyzer and the samples were degassed at 120 °C for 8 h under vacuum (10^{-5} bar) before analysis. The pore size distributions were calculated from the N_2 adsorption branch with the nonlocal density functional theory (NLDFT). The product of photocatalytic reaction was monitored by GC-MS (Shimadzu GCQP 2010SE). The chromatographic column used in this method is Rtx-5MS (solvent: dichloromethane, solvent delay: 4 min). Electron paramagnetic resonance (EPR) spectra were conducted on Bruker A300. CHI-760E electrochemical workstation (CH Instruments, USA) with three-electrode system was used to perform electrochemical measurements (working electrode: the glass carbon electrode, counter electrode: platinum wire electrode and reference electrode: saturated calomel electrode).

2.3. General procedures for photocatalytic Povarov reaction

When a mixture of 1-phenyl-1H-pyrrole-2,5-dione (0.1 mmol), *N,N*-dimethylaniline (0.2 mmol) and QA-TAPT-COF (10 mmol%) in 1.0 mL DMF was irradiated using a Xe lamp ($\lambda > 400$ nm, 300 W) under O_2 atmosphere, and the tetrahydroquinoline product was generated after 45 min. The reaction solution and the catalyst were separated by centrifugation, and the catalyst was washed with DMF and THF for several times. The reaction solution was poured into 10 mL saturated

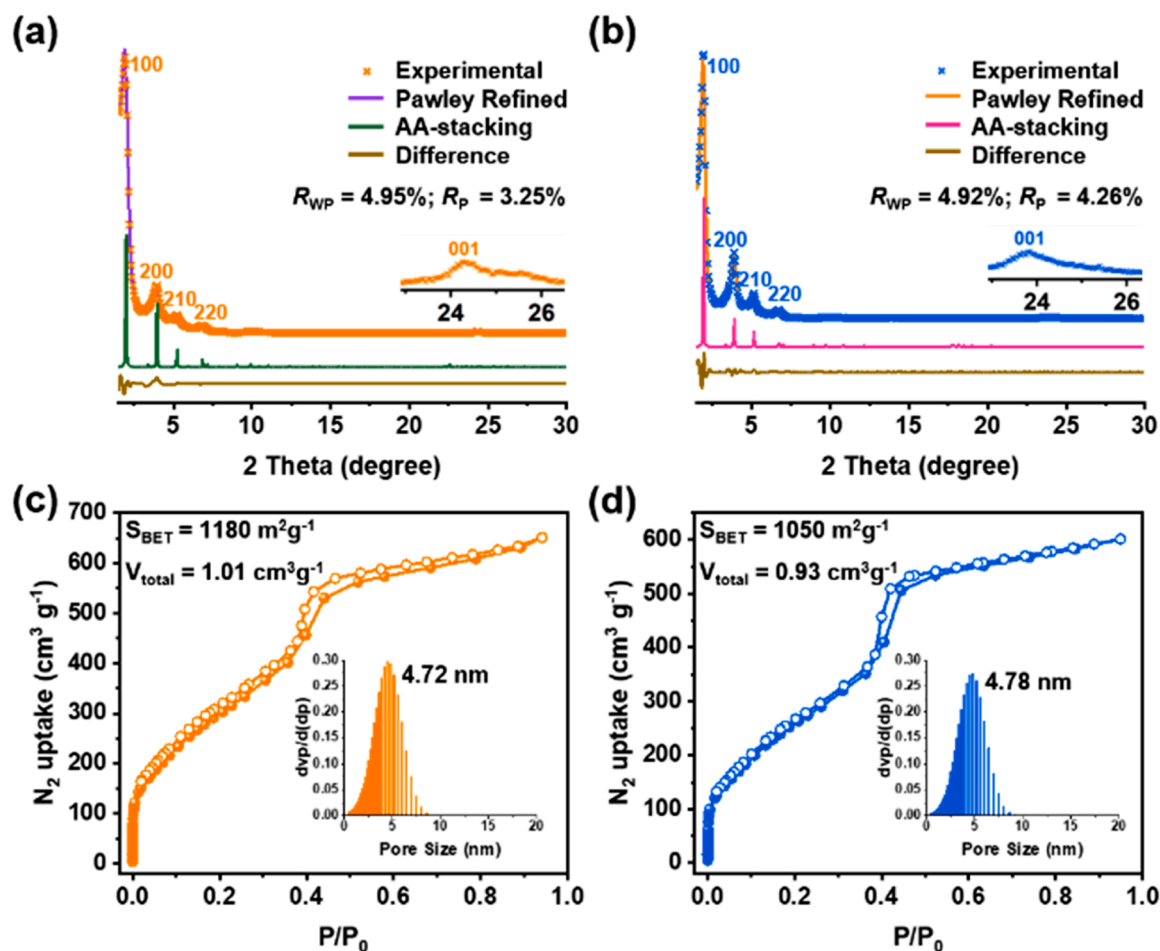


Fig. 1. The PXRD patterns of (a) QA-TAPT-COF and (b) QA-TPB-COF and its Pawley refinement, simulated pattern based on AA-stacking mode and difference between experimental and simulated results. The N_2 sorption isotherms of (c) QA-TAPT-COF and (d) QA-TPB-COF (inset: pore size distribution).

brine and extracted with dichloromethane (DCM). The organic phase was combined and dried over anhydrous $MgSO_4$ and then filtered. The solvent was removed under reduced pressure. Finally, the crude product was purified through silica gel column (eluent: petroleum ether: DCM = 3:2).

3. Results and discussion

3.1. Structural Characterization

Herein, QA-PCHO was synthesized via *N*-arylation of benzene halide and quinacridone (Scheme 1a), which was easier to be obtained than unprotected QA-monomer (QA-CHO). QA-PCHO and QA-CHO were characterized by 1H , ^{13}C and high-resolution mass spectra (Figs. S20–S25). Different from common linear bitopic monomer, QA-PCHO adopts a zigzag configuration which could enrich eventual structural diversity of the corresponding COFs. Polycondensation of QA-PCHO with two tritopic amine monomers (TAPT and TAPB) under solvothermal conditions afford two QA-based imine COFs (QA-TAPT-COF and QA-TPB-COF, Scheme 1b) and are insoluble in common organic solvents. Furthermore, we also performed the synthesis of QA-TAPT-COF using QA-CHO under solvothermal conditions. Compared with QA-TAPT-COF synthesized from QA-PCHO, the target COF from QA-CHO exhibited worse crystallinity (Figs. S1 and S2). Thus, QA-PCHO was directly used for QA-based COFs synthesis.

The chemical structures of two QA-based imine COFs were confirmed by Fourier transform infrared (FT-IR) and solid-state ^{13}C Cross-Polarization with total suppression of spinning sidebands (CP-

TOSS) spectroscopies. The FT-IR spectrum of QA-TAPT-COF exhibited an intense $C=O$ stretching vibration originated from QA units at 1631 cm^{-1} and $C=N$ stretching vibration of triazines at 1507 cm^{-1} , indicating QA and TAPT-moieties were successfully integrated into the skeleton [36]. In addition, the disappearance of aliphatic stretching bands ($2860\text{--}2950 \text{ cm}^{-1}$) and N-H stretching bands ($3500\text{--}3200 \text{ cm}^{-1}$) compared to their corresponding monomers reveals the high condensation efficiency of the building units (Fig. S3). Similarly, the chemical shifts at 175, 169 and 161 ppm in the solid-state ^{13}C Cross-polarization with total suppression of spinning sidebands (CP-TOSS) NMR spectrum of QA-TAPT-COF were assigned to the C of carbonyl groups of QA-units, triazine rings and imine bonds, respectively, which also demonstrated the formation of imine linkages and integration of QA-moieties in the framework (Fig. S4). Moreover, elemental analysis results indicated that the contents of C, H, N and O were in good accordance with the theoretical compositions of two QA-based COFs (Table S1). Field-emission scanning electron microscopy (FE-SEM) was employed to reveal the morphologies of two COFs. Both QA-TAPT-COF and QA-TPB-COF exhibited rod-like morphologies (Fig. S5). Moreover, lattice fringes were clearly observed for the two COFs by transmission electron microscopy (TEM) (Fig. S6). Notably, both COFs showcased high thermal stability as indicated by thermogravimetric analysis (TGA). Therein, QA-TAPT-COF and QA-TPB-COF were thermally stable up to 509 and 517°C under N_2 atmosphere, respectively (Fig. S7). Furthermore, the chemical stabilities were tested in different conditions like 0.1 M HCl aqueous solution, 6 M NaOH aqueous solution, boiling water and DMF, respectively. As shown in Figs. S8–S11, all samples maintained their crystallinity, porosity and chemical composition upon treatments in

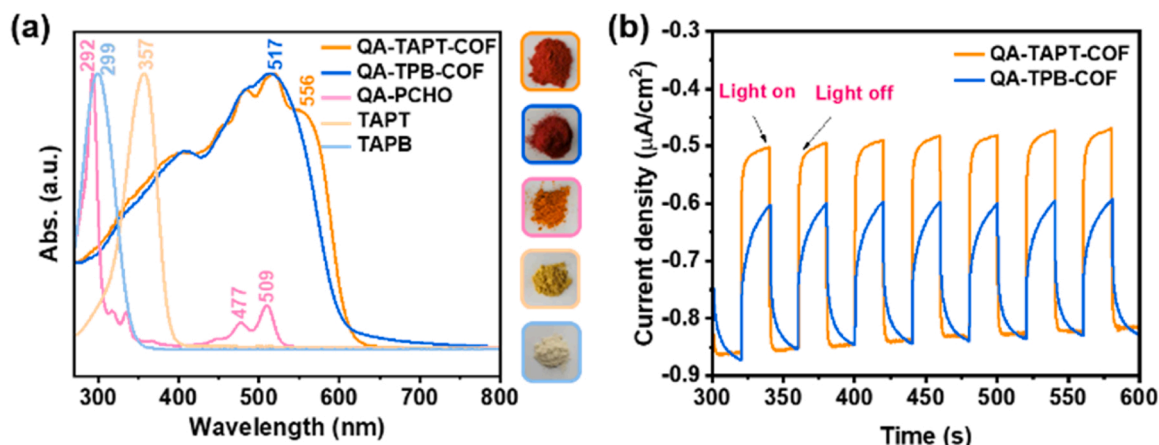


Fig. 2. (a) The UV-vis spectra of QA-PCHO, TAPB, TAPT in DMF (0.01 mM) and the solid-state diffuse reflectance UV-Vis spectra of QA-TAPT-COF and QA-TPB-COF. (b) Transient photocurrent responses of QA-TAPT-COF and QA-TPB-COF.

these conditions except in 0.1 M HCl aqueous solution, as indicated by PXRD, the FT-IR spectra and nitrogen sorption measurements. Besides, QA-TAPT-COF was irradiated by continuous light for 12 h using a Xenon lamp ($\lambda > 400$ nm, 300 W) could also maintain good crystallinity, chemical structures and permanent porosities as well.

The crystallinity of QA-TAPT-COF and QA-TPB-COF were examined by powder X-ray diffraction (PXRD) measurements. The PXRD pattern of QA-TAPT-COF exhibited a prominent diffraction peak at 1.95° with four minor peaks at 3.90° , 5.20° , 6.70° and 24.32° , corresponding to the (100), (200), (210), (220) and (001) facets respectively (Fig. 1a and S12a). The slipped AA-stacking and staggered AB-stacking mode were used to reconstruct the crystal structure of QA-TAPT-COF using Materials Studio package. As shown in Fig. 1a, the simulated PXRD pattern of AA-stacking mode reproduced the experimental profile very well. Pawley refinement of QA-TAPT-COF was agreed well with the AA-stacking model in a space group of $P6/M$ and afforded an optimized lattice parameter of $a = b = 51.47 \text{ \AA}$, $c = 3.87 \text{ \AA}$, $\alpha = \beta = 90^\circ$ and $\gamma = 120^\circ$ with $R_{\text{wp}} = 4.95\%$ and $R_p = 3.25\%$. Similar simulation results were obtained for QA-TPB-COF and the unit cell parameters were calculated as $a = b = 51.62 \text{ \AA}$, $c = 3.67 \text{ \AA}$, $\alpha = \beta = 90^\circ$ and $\gamma = 120^\circ$ with $R_{\text{wp}} = 4.92\%$ and $R_p = 4.26\%$ optimized by lattice simulation and Pawley refinement (Fig. 1b and S13a).

The permanent porosities of QA-TAPT-COF and QA-TPB-COF were assessed by nitrogen sorption measurements at 77 K. The sorption profiles of both QA-TAPT-COF and QA-TPB-COF exhibited obvious type-IV characteristics with sharp sorption steps at $P/P_0 < 0.05$ and capillary condensation between $P/P_0 = 0.40\sim 0.45$ (Fig. 1c and d), which indicated both COFs are mesoporous. The Brunauer–Emmett–Teller (BET) surface areas of QA-TAPT-COF and QA-TPB-COF were calculated to be 1180 and $1050 \text{ m}^2 \text{ g}^{-1}$, respectively. The total pore volume (at $P/P_0 = 0.945$) were determined to be $1.01 \text{ cm}^3 \text{ g}^{-1}$ for QA-TAPT-COF and $0.93 \text{ cm}^3 \text{ g}^{-1}$ for QA-TPB-COF. Furthermore, both COFs exhibited narrow pore size distributions at 4.72 and 4.78 nm respectively calculated by nonlocal density functional theory (NLDFT), which was in good consistence with the theoretic values (4.80 and 4.86 nm) based on the AA-stacking model and the d -spacing values (4.40 and 4.42 nm) observed in the PXRD results. It can be concluded that QA unit with special zig-zag configuration is an effective building block for constructing large-pore COFs.

The UV-Vis spectra of monomers and the solid-state diffuse reflectance UV-vis spectra of corresponding COFs were measured and compared. QA-PCHO exhibited the ultraviolet absorption at 270–550 nm, where the absorption at 477 and 509 nm is ascribed to the characteristic absorption band of QA unit [37]. QA-TAPT-COF and QA-TPB-COF exhibited broad absorption in the range of 270–600 nm with maximum absorption wavelength at 556 and 517 nm, respectively.

Table 1
Optimization of the reaction conditions^a.

Entry	1a	Oxidant	2a	Light source	Catalyst	Solvent	3a	Conv. ^b (%)
1		O ₂		Xe lamp	QA-TAPT-COF	DMF		> 99
2		O ₂		Xe lamp	QA-TAPT-COF	MeOH		12
3		O ₂		Xe lamp	QA-TAPT-COF	CH ₃ CN		27
4		O ₂		none	QA-TAPT-COF	DMF		N. D. ^c
5		N ₂		Xe lamp	QA-TAPT-COF	DMF		trace
6		O ₂		Xe lamp	none	DMF		N. D.
7		air		Xe lamp	QA-TAPT-COF	DMF		34
8		O ₂		Xe lamp	QA-TPB-COF	DMF		84
9		O ₂		Xe lamp	QA-TAPT-Polymer ^d	DMF		71
10		O ₂		Xe lamp	DPQA ^e	DMF		59
11		O ₂		Xe lamp	TAPB	DMF		26
12		O ₂		Xe lamp	TAPT	DMF		44

^a Reaction condition: 1a (0.1 mmol), 2a (0.2 mmol), catalyst (10 mmol%), solvent (1.0 mL), Xe lamp ($\lambda > 400$ nm, 300 W), O₂ balloon, room temperature, 45 min.

^b Conversion efficiency was calculated based on GC-MS. Conversion = [Consumed maleimide]/[Initial maleimide] \times 100%.

^c N. D. = The product was not detected by GC-MS.

^d QA-TAPT-Polymer is amorphous QA-TAPT-COF.

^e *N,N*-diphenyl quinacridone synthesized by quinacridone and iodobenzene.

The extended and conjugated structure of COFs linked by imine bonds led to the red shift in the absorption compared to the corresponding monomers (Fig. 2a). Additionally, based on the Kubelka–Munk–transformed reflectance spectra, the optical band gaps of QA-TAPT-COF and QA-TPB-COF were estimated as 2.03 and 2.09 eV, respectively. (Fig. S14c). The highest occupied molecular orbital (HOMO) energy levels of QA-TAPT-COF and QA-TPB-COF were calculated to be -5.19 and -5.14 eV based on the cyclic voltammetry (CV) results (Figs. S14a and S14b). And the corresponding lowest unoccupied molecular orbital (LUMO) energy levels were -3.16 and -3.05 eV for QA-TAPT-COF and QA-TPB-COF, calculated by HOMO levels and optical band gaps (Fig. S14d).

3.2. Photocatalytic properties

Povarov reaction is a facile and effective method for the synthesis of tetrahydroquinoline, which has been frequently studied as antipsychotic and analgesic agents [38]. This reaction is generally catalyzed by

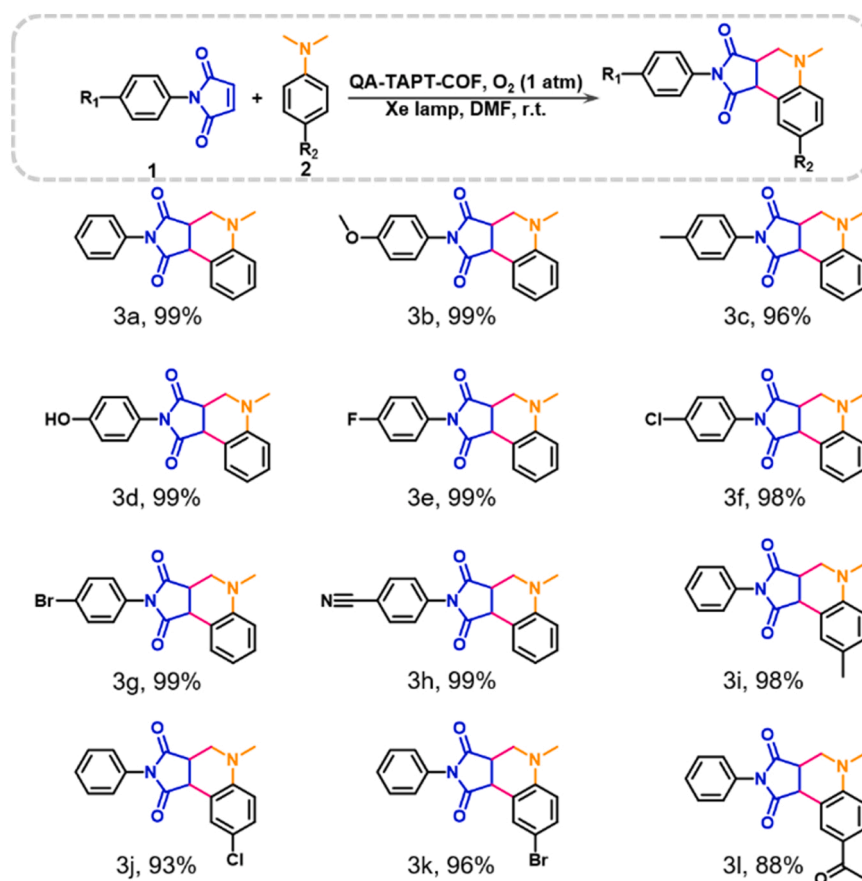


Fig. 3. Catalytic aerobic oxidation of maleimide and *N,N*-dimethylaniline. Reactions were carried out using 0.1 mmol of substrates 1, 0.2 mmol substrate 2 and 7.0 mg QA-TAPT-COF.

transition metal-based complexes and dyes, which will cause environmental pollution due to their nondegradability and toxicity. Featuring large porosity, strong absorption in visible light, non-toxicity and recyclability, QA-based 2D COFs were thus explored as the photocatalysts for Povarov reaction [39–44]. First, maleimide (**1a**) and *N,N*-dimethylaniline (**2a**) were initially tested as the substrates. QA-TAPT-COF was explored as the photocatalyst using molecular oxygen as a green oxidant under Xe lamp ($\lambda > 400$ nm, 300 W) irradiation at room temperature to screen the solvents (e.g. DMF, MeOH, CH₃CN in Table 1, entries 1, 2 and 3). And an optimized conversion efficiency of 99% was achieved in the single solvent of DMF. To better understand the catalytic mechanism, a series of systematic control experiments were conducted to reveal the factors affecting this reaction and the results are summarized in Table 1. As revealed in entries 4 and 5 (Table 1), the reaction did not occur in the absence of visible light irradiation or oxygen with QA-TAPT-COF as the catalyst. On the other hand, no product was detected in the absence of QA-TAPT-COF under oxygen atmosphere (entry 6). These results demonstrated that light, molecular oxygen and QA-TAPT-COF are all indispensable in this chemical transformation. Interestingly, when the photocatalytic reaction was performed under air instead of pure oxygen atmosphere, only 34% conversion was obtained (entry 7). Additionally, QA-TPB-COF could also catalyze the oxidative cyclization but with much inferior efficiency (Table 1, entry 8). By analysing the electrochemical impedance spectroscopy (EIS) of two COFs, it was found that QA-TAPT-COF has a smaller capacitive arc radius, which revealed the charge transfer barrier of QA-TAPT-COF was reduced (Fig. S15).

Meanwhile, the transient photocurrent intensity of QA-TAPT-COF was higher than that of QA-TPB-COF under the same conditions, which indicated QA-TAPT-COF was more responsive to light (Fig. 2b).

These results collectively demonstrated that QA-TAPT-COF outperforms QA-TPB-COF in the catalysis of aerobic oxidation. To further confirm the key catalytic roles of QA-TAPT-COF toward this reaction, control experiments of using amorphous counterpart of QA-TAPT-Polymer and three different monomers as the photocatalysts were performed under the same conditions. As listed in Table 1 (entry 9), the QA-TAPT-Polymer was less efficient with worse conversion efficiency of 71% under same reaction conditions, which proved that the crystallinity and ordered structures are also conducive to the catalysis. Due to the lack of open active sites and large conjugated skeleton, the catalytic efficiency of the oxidative cyclization using *N,N*-diphenyl quinacridone (DPQA), TAPT and TPB was unsatisfying (entries 10–12).

With optimal condition for the aerobic oxidation catalyzed by QA-TAPT-COF in hand, the substrate scope by using different substituted *N*-phenylmaleimides (**1**) and *N,N*-dimethylaniline (**2**) was further explored (Fig. 3). A series of electronically differentiated substituted maleimide were found to afford the target products **3b–3h** in good conversion (> 96%) when *N,N*-dimethylaniline (**2a**) was employed as the substrate. To our delight, excellent functional-group compatibility was realized for methyl, hydroxyl and halogen (F, Cl and Br) groups. Substrates with electron-donating (methoxy) and electron-withdrawing (cyanide) were converted with excellent conversion, resulting in the formation of desired tetrahydroquinoline **3b** or **3h**, respectively. Furthermore, the scope of *N,N*-dimethylaniline (**2**) with different aryl substituents was also evaluated. The reaction was compatible with *N,N*-dimethylaniline that containing methyl or halogens (Cl and Br). In the case of strong electron-withdrawing acetyl substituent, the target compound **3l** was also obtained in decent conversion efficiency.

To further confirm the feasibility of QA-TAPT-COF toward this photocatalytic reaction, the recycling experiments were performed and

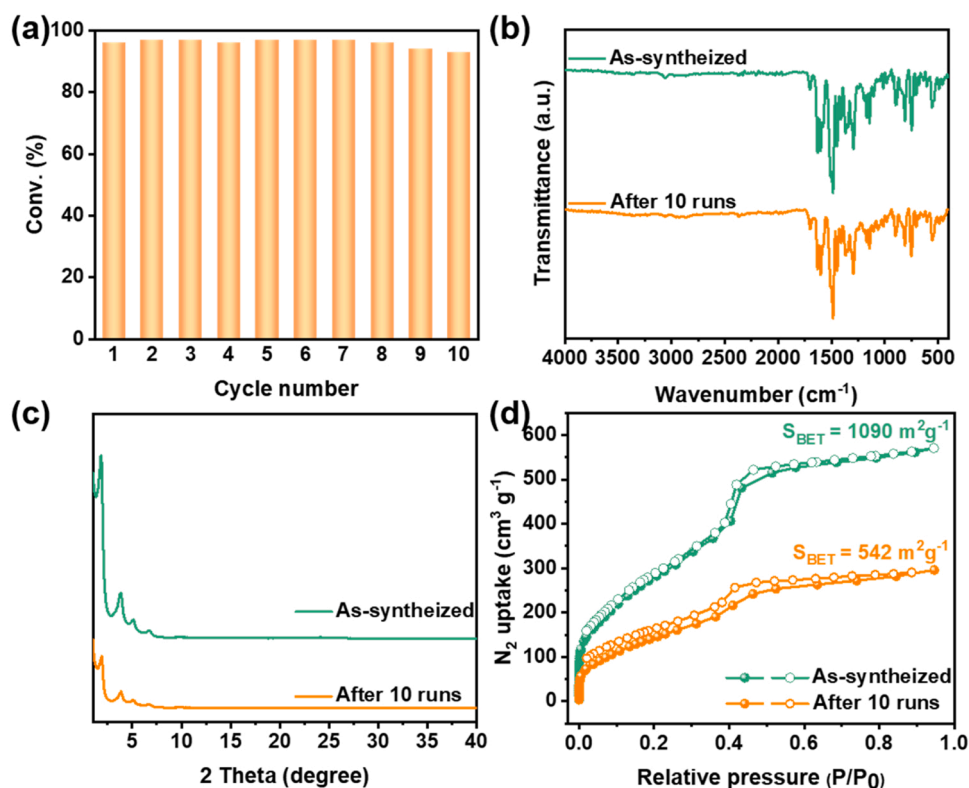


Fig. 4. (a) Assessment of the reusability of QA-TAPT-COF in recycling experiments. (b) FT-IR spectra, (c) PXRD patterns and (d) N_2 sorption isotherms of QA-TAPT-COF before and after the 10 cycles of photocatalysis.

the conversion could still be retained to 93% after at least 10 cycles (Fig. 4a). Furthermore, the chemical structure and crystallinity of QA-TAPT-COF could also be maintained after cycling, which was confirmed by FT-IR, PXRD and N_2 sorption measurements (Fig. 4b-c). To shed more insights into the photocatalytic process, the mechanism of the aerobic oxidation catalyzed by QA-TAPT-COF was investigated in details. A series of control experiments were performed, in which different kinds of scavengers were added separately to the reaction systems for identifying the actual reactive species. As show in Fig. S16, the addition of $\cdot OH$ radical scavenger (isopropanol) and H_2O_2 scavenger (catalase) only resulted in a slight decrease of the conversion efficiency, while the addition of free holes (h^+) scavenger (ammonium oxalate) and $O_2^{\cdot -}$ scavenger (benzoquinone) resulted in significant decrease of conversion. To further verify the generation of active $O_2^{\cdot -}$, 5,5-dimethyl-1-pyrroline *N*-oxide (DMPO) was used as the trapping agent, and the formation of the intermediate of DMPO- $O_2^{\cdot -}$ was monitored by electron paramagnetic resonance (EPR). As shown in Fig. S17, QA-TAPT-COF shows characteristic EPR signal of DMPO- $O_2^{\cdot -}$ at $g = 2.0087$, further proving the generation of $O_2^{\cdot -}$. Combining the photocatalytic behavior of QA-TAPT-COF with previous reports on the aerobic oxidation [45], a plausible mechanism of aerobic oxidation based on the maleimide (1) and *N,N*-dimethylaniline (2) as substrate was proposed (Fig. S18). Firstly, charge separation would occur in QA-TAPT-COF upon light irradiation to generated free h^+ and electrons, and O_2 was subsequently reduced by the separated charges to generate $O_2^{\cdot -}$. *N,N*-dimethylaniline was oxidated by h^+ and transferred protons to $O_2^{\cdot -}$. The resulted α -aminoalkyl radicals react with the ethylene groups of maleimide and eventually formed tetrahydroquinoline after cyclization and oxidation of HO_2^{\cdot} .

4. Conclusion

In summary, we designed and synthesized a new monomer with zigzag configuration significantly different from other reported C_2 -symmetric monomers. The polycondensation of QA-PCHO and two

tritopic amines (TAPT or TAPB) afforded two QA-based COFs with large pore size (> 4.7 nm). Regarding to the configuration and optical activity of densely and uniformly distributed quinacridone in the skeletons, the QA-based COFs not only enrich the structural diversity of COFs library but also demonstrate outstanding performance in aerobic oxidative Povarov reaction as the photocatalysts. Furthermore, QA-PCHO could also be reacted with tetratopic amino derivatives to construct new COFs with *sql* net structures and applied as photoresponsive materials, which are currently in progress in our laboratory.

CRediT authorship contribution statement

Zilin Liu: Investigation, Data curation, Formal analysis, Writing – review & editing. **Xiao Yang:** Data curation, Formal analysis. **Zongfan Yang:** Investigation, Formal analysis, Writing – review & editing. **Xi Su:** Data curation, Formal analysis. **Zhen Xie:** Software, Formal analysis. **Weihua Chen:** Investigation, Formal analysis, Writing – review & editing. **Wenqin Zhang:** Methodology, Writing – review & editing. **Long Chen:** Conceptualization, Writing – original draft, Supervision, Funding acquisition.

Declaration of Competing Interest

The authors declare that they have no known competing financial interests or personal relationships that could have appeared to influence the work reported in this paper.

Acknowledgment

This work was financially supported by the National Natural Science Foundation of China (51973153).

Appendix A. Supporting information

Supplementary data associated with this article can be found in the online version at doi:10.1016/j.apcatb.2022.121406.

References

- [1] R. Liu, K.T. Tan, Y. Gong, Y. Chen, Z. Li, S. Xie, T. He, Z. Lu, H. Yang, D. Jiang, Covalent organic frameworks: an ideal platform for designing ordered materials and advanced applications, *Chem. Soc. Rev.* 50 (2021) 120–242.
- [2] D. Chen, W. Chen, G. Zhang, S. Li, W. Chen, G. Xing, L. Chen, N-rich 2D heptazine covalent organic frameworks as efficient metal-free photocatalysts, *ACS Catal.* 12 (2022) 616–623.
- [3] S. Bi, P. Thiruvengadam, S. Wei, W. Zhang, F. Zhang, L. Gao, J. Xu, D. Wu, J. S. Chen, F. Zhang, Vinylene-bridged two-dimensional covalent organic frameworks via Knoevenagel condensation of tricyanomesitylene, *J. Am. Chem. Soc.* 142 (2020) 11893–11900.
- [4] W. Hao, D. Chen, Y. Li, Z. Yang, G. Xing, J. Li, L. Chen, Facile synthesis of porphyrin based covalent organic frameworks via an A₂B₂ monomer for highly efficient heterogeneous catalysis, *Chem. Mater.* 31 (2019) 8100–8105.
- [5] Q. Sun, B. Aguila, J. Perman, N. Nguyen, S. Ma, Flexibility matters: cooperative active sites in covalent organic framework and threaded ionic polymer, *J. Am. Chem. Soc.* 138 (2016) 15790–15796.
- [6] X. Wang, X. Han, J. Zhang, X. Wu, Y. Liu, Y. Cui, Homochiral 2D porous covalent organic frameworks for heterogeneous asymmetric catalysis, *J. Am. Chem. Soc.* 138 (2016) 12332–12335.
- [7] Z. Zhang, J. Jia, Y. Zhi, S. Ma, X. Liu, Porous organic polymers for light-driven organic transformations, *Chem. Soc. Rev.* 51 (2022) 2444–2490.
- [8] K. Geng, T. He, R. Liu, S. Dalapati, K.T. Tan, Z. Li, S. Tao, Y. Gong, Q. Jiang, D. Jiang, Covalent organic frameworks: design, synthesis, and functions, *Chem. Rev.* 120 (2020) 8814–8933.
- [9] Y. Lv, Y. Li, G. Zhang, Z. Peng, L. Ye, Y. Chen, T. Zhang, G. Xing, L. Chen, An in situ film-to-film transformation approach toward highly crystalline covalent organic framework films, *CCS Chem.* 3 (2021) 1773–1779.
- [10] X. Wang, P. She, Q. Zhang, Recent advances on electrochemical methods in fabricating two-dimensional organic-ligand-containing frameworks, *SmartMat* 2 (2021) 299–325.
- [11] H. Lyu, C.S. Diercks, C. Zhu, O.M. Yaghi, Porous crystalline olefin-linked covalent organic frameworks, *J. Am. Chem. Soc.* 141 (2019) 6848–6852.
- [12] T. Sick, A.G. Hufnagel, J. Kampmann, I. Kondofersky, M. Calik, J.M. Rotter, A. Evans, M. Doblinger, S. Herbert, K. Peters, D. Bohm, P. Knochel, D.D. Medina, D. Fattakhova-Rohlfing, T. Bein, Oriented films of conjugated 2D covalent organic frameworks as photocathodes for water splitting, *J. Am. Chem. Soc.* 140 (2018) 2085–2092.
- [13] D. Bessinger, L. Ascherl, F. Auras, T. Bein, Spectrally switchable photodetection with near-infrared-absorbing covalent organic frameworks, *J. Am. Chem. Soc.* 139 (2017) 12035–12042.
- [14] V.S. Vyas, F. Haase, L. Stegbauer, G. Savasci, F. Podjaski, C. Ochsenfeld, B. V. Lotsch, A tunable azine covalent organic framework platform for visible light-induced hydrogen generation, *Nat. Commun.* 6 (2015) 8508.
- [15] S.-Y. Ding, J. Gao, Q. Wang, Y. Zhang, W.-G. Song, C.-Y. Su, W. Wang, Construction of covalent organic framework for catalysis: Pd/COF-LZU1 in Suzuki–Miyaura coupling reaction, *J. Am. Chem. Soc.* 133 (2011) 19816–19822.
- [16] C.H. Yang, J.S. Chang, D.J. Lee, Covalent organic framework EB-COF:Br as adsorbent for phosphorus (V) or arsenic (V) removal from nearly neutral waters, *Chemosphere* 253 (2020) 126736.
- [17] H. Zhang, L.L. Lou, K. Yu, S. Liu, Advances in chiral metal-organic and covalent organic frameworks for asymmetric catalysis, *Small* 17 (2021), 2005686.
- [18] S. Lu, Y. Hu, S. Wan, R. McCaffrey, Y. Jin, H. Gu, W. Zhang, Synthesis of ultrafine and highly dispersed metal nanoparticles confined in a thioether-containing covalent organic framework and their catalytic applications, *J. Am. Chem. Soc.* 139 (2017) 17082–17088.
- [19] W. Chen, L. Wang, D. Mo, F. He, Z. Wen, X. Wu, H. Xu, L. Chen, Modulating benzothiadiazole-based covalent organic frameworks via halogenation for enhanced photocatalytic water splitting, *Angew. Chem. Int. Ed.* 59 (2020) 16902–16909.
- [20] X. Zhao, P. Pachfule, S. Li, T. Langenhahn, M. Ye, C. Schlesiger, S. Praetz, J. Schmidt, A. Thomas, Macro/Microporous covalent organic frameworks for efficient electrocatalysis, *J. Am. Chem. Soc.* 141 (2019) 6623–6630.
- [21] M. Li, J. Liu, Y. Li, G. Xing, X. Yu, C. Peng, L. Chen, Skeleton engineering of isostructural 2D covalent organic frameworks: orthoquinone redox-active sites enhanced energy storage, *CCS Chem.* 3 (2021) 696–706.
- [22] T. Hisatomi, K. Domen, Reaction systems for solar hydrogen production via water splitting with particulate semiconductor photocatalysts, *Nat. Catalysis* 2 (2019) 387–399.
- [23] T. Banerjee, K. Gottschling, G. Savasci, C. Ochsenfeld, B.V. Lotsch, H₂ Evolution with covalent organic framework photocatalysts, *ACS Energy Lett.* 3 (2018) 400–409.
- [24] T. Zhang, G. Zhang, L. Chen, 2D conjugated covalent organic frameworks: defined synthesis and tailor-made functions, *Acc. Chem. Res.* 55 (2022) 795–808.
- [25] T. Xu, S. An, C. Peng, J. Hu, H. Liu, Construction of large-pore crystalline covalent organic framework as high-performance adsorbent for rhodamine B dye removal, *Ind. Eng. Chem. Res.* 59 (2020) 8315–8322.
- [26] S.T. Emmerling, R. Schults, S. Bette, L. Yao, R.E. Dinnebier, J. Kastner, B.V. Lotsch, Interlayer interactions as design tool for large-pore COFs, *J. Am. Chem. Soc.* 143 (2021) 15711–15722.
- [27] J. Jia, T. Li, Y. Cui, Y. Li, W. Wang, L. Han, Y. Li, J. Gao, Study on the synthesis and third-order nonlinear optical properties of D-A poly-quinacridone optical materials, *Dyes Pigments* 162 (2019) 26–35.
- [28] J. Gao, C. Strässler, D. Tahmassebi, E.T. Kool, Libraries of composite polyfluors built from fluorescent deoxyribosides, *J. Am. Chem. Soc.* 124 (2002) 11590–11591.
- [29] M. Xu, K. Kong, H. Ding, Y. Chu, S. Zhang, F. Yu, H. Ye, Y. Hu, J. Hua, Quinacridone-pyridine dicarboxylic acid based donor–acceptor supramolecular nanobelt for significantly enhanced photocatalytic hydrogen production, *J. Mater. Chem. C* 8 (2020) 930–934.
- [30] X. Yu, F. Wen, F. Zhang, P. Yang, Y. Zhao, Y. Wu, Y. Wang, Z. Liu, Photocatalytic reduction of CO₂ to CO over quinacridone-BiVO₄ nanocomposites, *ChemSusChem* 13 (2020) 5565–5570.
- [31] Y. Qu, Y. Jin, Y. Cheng, L. Wang, J. Cao, J. Yang, A solthiocarbonyl quinacridone with long chains used as a fluorescent tool for rapid detection of Hg²⁺ in hydrophobic naphtha samples, *J. Mater. Chem. A* 5 (2017) 14537–14541.
- [32] C. Sakong, S.-H. Kim, S.-B. Yuk, J.-Y. Kim, S.-W. Park, M.-J. Ko, J.-P. Kim, Synthesis of novel quinacridone dyes and their photovoltaic performances in organic dye-sensitized solar cells, *Bull. Korean Chem. Soc.* 32 (2011) 2553–2559.
- [33] J.J.-A. Chen, T.L. Chen, B. Kim, D.A. Poulsen, J.L. Mynar, J.M.J. Fréchet, B. Ma, Quinacridone-based molecular donors for solution processed bulk-heterojunction organic solar cells, *ACS Appl. Mater. Interfaces* 2 (2010) 2679–2686.
- [34] H. Min, I.S. Park, T. Yasuda, cis-Quinacridone-based delayed fluorescence emitters: seemingly old but renewed functional luminogens, *Angew. Chem. Int. Ed.* 60 (2021) 7643–7648.
- [35] C. Wang, Z. Zhang, Y. Wang, Quinacridone-based π -conjugated electronic materials, *J. Mater. Chem. C* 4 (2016) 9918–9936.
- [36] C. Rădulescu, I. Ioniță, A.M. Hossu, Synthesis of linear bis-thiazolo[2,3-d][8,9-d] trans-quinacridone, *Dyes Pigments* 65 (2005) 175–177.
- [37] J. Jia, D. Feng, Y. Sha, C. Zhou, G. Liang, Y. She, New quinacridone derivatives: Synthesis, photophysical and third-order nonlinear optical properties, *Tetrahedron* 76 (2020) 131057–131066.
- [38] S. Firoozi, M. Hosseini-Sarvari, M. Koohgard, Solvent-free and room temperature visible light-induced C–H activation: CdS as a highly efficient photo-induced reusable nano-catalyst for the C–H functionalization cyclization of *t*-amines and C–C double and triple bonds, *Green Chem.* 20 (2018) 5540–5549.
- [39] Z. Almansaf, J. Hu, F. Zanca, H.R. Shahsavari, B. Kampmeyer, M. Tsuji, K. Maity, Y. Lomonte, Y. Ha, P. Mastroianni, S. Todisco, M. Benamara, R. Oktavian, A. Mirjafari, P.Z. Moghadam, A.R. Khosropour, H. Beyzavi, Pt(II)-Decorated covalent organic framework for photocatalytic difluoroalkylation and oxidative cyclization reactions, *ACS Appl. Mater. Interfaces* 13 (2021) 6349–6358.
- [40] X. Yang, T. Liang, J. Sun, M.J. Zaworotko, Y. Chen, P. Cheng, Z. Zhang, Template-directed synthesis of photocatalyst-encapsulating metal–organic frameworks with boosted photocatalytic activity, *ACS Catal.* 9 (2019) 7486–7493.
- [41] R. Li, J. Byun, W. Huang, C. Ayed, L. Wang, K.A.I. Zhang, Poly(benzothiadiazoles) and their derivatives as heterogeneous photocatalysts for visible-light-driven chemical transformations, *ACS Catal.* 8 (2018) 4735–4750.
- [42] J. Tang, G. Grampp, Y. Liu, B.X. Wang, F.F. Tao, L.J. Wang, X.Z. Liang, H.Q. Xiao, Y.M. Shen, Visible light mediated cyclization of tertiary anilines with maleimides using nickel(II) oxide surface-modified titanium dioxide catalyst, *J. Org. Chem.* 80 (2015) 2724–2732.
- [43] Z. Liang, S. Xu, W. Tian, R. Zhang, Eosin Y-catalyzed visible-light-mediated aerobic oxidative cyclization of *N,N*-dimethylanilines with maleimides, *Beilstein J. Org. Chem.* 11 (2015) 425–430.
- [44] X. Ju, D. Li, W. Li, W. Yu, F. Bian, The reaction of tertiary anilines with maleimides under visible light redox catalysis, *Adv. Synth. Catal.* 354 (2012) 3561–3567.
- [45] Z.J. Wang, S. Ghasimi, K. Landfester, K.A.I. Zhang, Bandgap engineering of conjugated nanoporous poly-benzobisthiadiazoles via copolymerization for enhanced photocatalytic 1,2,3,4-tetrahydroquinoline synthesis under visible light, *Adv. Synth. Catal.* 358 (2016) 2576–2582.